

Article

Highly Efficient Cobalt Sulfide Heterostructures Fabricated on Nickel Foam Electrodes for Oxygen Evolution Reaction in Alkaline Water Electrolysis Cells

Ioannis Poimenidis ^{1,*}, Nikandra Papakosta ^{2,3}, Panagiotis A. Loukakos ², George E. Marnellos ^{4,5} and Michalis Konsolakis ^{1,*}

¹ Lab of Matter Structure and Laser Physics, School of Production Engineering & Management, Technical University of Crete, 73100 Chania, Crete, Greece

² Foundation for Research and Technology–Hellas, Institute of Electronic Structure and Laser, 70013 Heraklion, Greece; papakosta@iesl.forth.gr (N.P.); loukakos@iesl.forth.gr (P.A.L.)

³ Department of Materials Science and Technology, University of Crete, Vassilika Vouton, 70013 Heraklion, Greece

⁴ Department of Chemical Engineering, Aristotle University of Thessaloniki, 54124 Thessaloniki, Greece; gmarnellos@cheng.auth.gr or

⁵ Chemical Process and Energy Resources Institute, Centre for Research & Technology Hellas, 57001 Thessaloniki, Greece

* Correspondence: ipoimenidis@tuc.gr (I.P.); mkonsolakis@tuc.gr (M.K.)

Abstract: Non-noble metal electrocatalysts for the oxygen evolution reaction (OER) have recently gained particular attention. In the present work, a facile one-step electrodeposition method is applied in situ to synthesize cobalt sulfide nanostructures on nickel foam (NF) electrodes. For the first time, a systematic study is carried out on the impact of the Co/S molar ratio on the structural, morphological, and electrochemical characteristics of Ni-based OER electrodes by employing $\text{Co}(\text{NO}_3)_2 \cdot 6 \text{H}_2\text{O}$ and $\text{CH}_4\text{N}_2\text{S}$ as Co and S precursors, respectively. The optimum performance was obtained for an equimolar Co:S ratio (1:1), whereas sulfur-rich or Co-rich electrodes resulted in an inferior behavior. In particular, the $\text{Co}_x\text{S}_y/\text{NF}$ electrode with Co/S (1:1) exhibited the lowest overpotential value at 10 mA cm^{-2} (0.28 V) and a Tafel slope of 95 mV dec^{-1} , offering, in addition, a high double-layer capacitance (C_{DL}) of 10.7 mF cm^{-2} . Electrochemical impedance spectroscopy (EIS) measurements confirmed the crucial effect of the Co/S ratio on the charge-transfer reaction rate, which is maximized for a Co:S molar ratio of 1:1. Moreover, field emission scanning electron microscopy (FE-SEM), X-ray diffraction (XRD) and X-ray fluorescence (XRF) were conducted to gain insights into the impact of the Co/S ratio on the structural and morphological characteristics of the electrodes. Notably, the $\text{Co}_x\text{S}_y/\text{NF}$ electrocatalyst with an equimolar Co:S ratio presented a 3D flower-like nanosheet morphology, offering an increased electrochemically active surface area (ESCA) and improved OER kinetics.

Keywords: alkaline electrolysis; oxygen evolution reaction; electrodeposition on Ni foam; cobalt–sulfur molar ratio; thiourea



Citation: Poimenidis, I.; Papakosta, N.; Loukakos, P.A.; Marnellos, G.E.; Konsolakis, M. Highly Efficient Cobalt Sulfide Heterostructures Fabricated on Nickel Foam Electrodes for Oxygen Evolution Reaction in Alkaline Water Electrolysis Cells. *Surfaces* **2023**, *6*, 493–508. <https://doi.org/10.3390/surfaces6040033>

Academic Editor: Gaetano Granozzi

Received: 8 October 2023

Revised: 7 November 2023

Accepted: 16 November 2023

Published: 23 November 2023



Copyright: © 2023 by the authors. Licensee MDPI, Basel, Switzerland. This article is an open access article distributed under the terms and conditions of the Creative Commons Attribution (CC BY) license (<https://creativecommons.org/licenses/by/4.0/>).

1. Introduction

The fossil fuel crisis and global climate change have led researchers to pay increased attention to alternative energy sources. Hydrogen has great potential to be employed as an energy carrier for the forthcoming energy transition due to its high gravimetric energy density and zero carbon content [1–4]. In this regard, the electrochemical splitting of water using energy derived from intermittent renewable energy sources (green Hydrogen), such as photocatalysis, solar thermochemical, photovoltaic electrolysis, and the supercritical water gasification of biomass, has recently gained particular importance [5].

The maturity of the electrochemical water splitting process will highly contribute to the need for green hydrogen production in the years to come, which, according to the International Energy Agency analysis, will be ~150 Mt and ~435 Mt of low-carbon hydrogen production in 2030 and 2045, respectively [5].

However, it is well known that the efficiency of water electrolysis is associated with the overpotentials of the hydrogen evolution reaction (HER) and oxygen evolution reaction (OER) [6,7]. The high overpotential of the OER ($4\text{OH}^- \rightarrow 2\text{H}_2\text{O} + 4\text{e}^- + \text{O}_2$ in alkaline medium), due to the demanding transfer of four electrons in the anodic charge transfer reaction, represents the main bottleneck for the limited efficiencies [8–11]. The state-of-the-art electrodes used in the OER mainly comprise Ir and Ru metals; however, their scarcity and high cost notably hinder their widespread application as electrocatalysts [12–14].

Significant research has recently been devoted to noble-metal-free and earth-abundant transition metal electrocatalysts [15]. Various materials, such as borides, chalcogenides, etc., have been explored for the OER. However, most of these candidates suffer from a small active electrochemical area and low electrical conductivity, negatively affecting OER kinetics [15]. Recently, the in situ growth of nanostructured catalytic materials on conductive substrates, such as nickel foam (NF), has proven an efficient approach to overcoming these obstacles [15,16].

In recent years, transition-metal-based electrocatalysts have been developed for water splitting via various techniques, such as aerosol spray [17], photochemical metal–organic deposition [18], hydrothermal processes [19–22], pulsed laser deposition [23], etc. Among them, transition metal sulfides (TMSs) have been considered excellent alternatives for the OER due to their low cost, adjustable electronic properties, and adequate conductivity, which make them suitable alternatives to the Ru and IrO_2 benchmark electrodes [24–26].

Although various studies have been conducted using TMSs, especially with Co_xS_y composites, there is no systematic study on the impact of the sulfur/cobalt molar ratio on the electrochemical performance of electrocatalysts. Nonetheless, the type and concentration of the precursor compounds employed during fabrication are expected to affect the structural, morphological, and electrochemical properties of the electrocatalysts. Furthermore, in most studies, the fabricated electrocatalysts are in the form of powders, rendering the use of binders for the electrocatalyst's anchor to the substrate unavoidable, thus increasing the contact resistance [16,27]. In this regard, developing a facile and binder-free preparation protocol for highly efficient OER electrodes is paramount.

Motivated by the above challenges, the present work aims to investigate the effect of the sulfur/cobalt ratio on the OER. Although several studies have been devoted to cobalt sulfide electrocatalysts, there is no systematic study on the impact of sulfur/cobalt on their physicochemical properties and, in turn, on their OER performance. In this regard, a facile one-step electrodeposition method was used to fabricate Co_xS_y ($x:y$ molar ratio) binary electrodes on a nickel foam substrate (NF), employing thiourea ($\text{CH}_4\text{N}_2\text{S}$) and cobalt nitrate hexahydrate ($\text{Co}(\text{NO}_3)_2 \cdot 6\text{H}_2\text{O}$) as precursors. Various Co:S molar ratios were used during the electrodeposition process, and it was clearly disclosed that the Co:S ratio significantly affects the morphological and structural properties of the electrode and its electrochemical performance. Remarkably, the Co_xS_y @NF electrode with an equimolar Co:S ratio (1:1) presented the lowest overpotential values at 10 mA cm^{-2} (0.28 V), the lowest Tafel slope (95 mV dec^{-1}), and the highest C_{DL} (10.7 mF cm^{-2}) and ECSA (537 cm^2) values. On the other hand, sulfur-rich or Co-rich electrodes resulted in an inferior behavior, demonstrating the key effect of sulfur content on transition metal sulfide electrocatalysts.

2. Materials and Methods

2.1. Materials and Reagents

The chemical reagents in this work were used as received. Thiourea (98% Penta Chemical, Czech Republic-Prague), KOH (technical grade, Sigma-Aldrich, USA-VT-Burlington), ethanol (99.8%, ACROS Organics, Belgium-Antwerp), HCl (98% Sigma Aldrich), $\text{Co}(\text{NO}_3)_2 \cdot 6$

H₂O (Sigma-Aldrich) and nickel foam (99.8%, Beike advanced materials Store, China-Taizhou) were used as the electrodeposition substrate.

2.2. Electrodeposition on NF Substrate

The electrodeposition process was carried out by using an electrochemical station (Princeton Applied Research, USA-TN-Oak Ridge, VersaSTAT 4) equipped with a standard three-electrode electrochemical cell (Palmsens, Netherlands-Utrecht). The reference electrode was an Ag/AgCl electrode (3.5M KCl) (Palmsens), the counter electrode was a Pt wire (99% Goodfellow, USA-UT-Lindon), and the working electrode was an NF substrate.

Prior to the electrodeposition, the NF substrates were ultrasonicated in 3 M HCl for 10 min to activate the substrate and remove any organic impurities. Then, it was rinsed with deionized water, ultrasonicated again for 10 min in pure ethanol, and finally rinsed with deionized water.

The electrodeposition for all the samples lasted 10 min at 298 K, and the applied potential was -0.18 V vs. RHE. For the uniform deposition of the nanomaterials, a magnetic stirrer was used. The molar ratio of the Co(NO₃)₂·6 H₂O and thiourea (CH₄N₂S) precursors during the synthesis procedure was varied in a wide range (i.e., 0:1, 1:0, 1:2, 1:1, 2:1, 4:1) to obtain both sulfur-rich and Co-rich electrodes. The as-prepared electrodes were defined as Co:S (x:y), where x:y represents the Co:S molar ratio of the CoS_x@NF composites, whereas the bare nickel foam substrate was designated as NF. Pure cobalt (Co:S (1:0)) and sulfur (Co:S (0:1)) electrodes on the NF substrate (1 × 1 cm) were also fabricated for comparison purposes. After electrodeposition, a calcination procedure was applied (at 250 °C in an air atmosphere) in order to increase the material's crystallinity and remove any surface impurities.

2.3. Structural and Morphological Characterization

The morphological characterization of the fabricated electrodes was carried out with field emission scanning electron microscopy (FE-SEM, JSM7000F, JEOL) at various magnification scales. Also, XRD (BEDE D1 with CuKα radiation) and XRF (Amptek X-123) analyses were conducted to gain insights into the structural features of the Co_xS_y@NF electrodes.

2.4. Electrochemical Evaluation of the Fabricated Electrodes

Electrochemical tests were undertaken for each developed electrode to assess its oxygen evolution reaction kinetics and electrochemical performance under water-alkaline electrolysis conditions. Specifically, cyclic voltammetry (CV), linear sweep voltammetry (LSV), and electrochemical impedance spectroscopy (EIS) measurements were carried out, and the values of the Tafel slope, double layer capacitance (C_{DL}), and ECSA were calculated. The above studies were accomplished using the VersaSTAT 4 electrochemical workstation, which was equipped with a Pt (99%) counter electrode and an Ag/AgCl (3.5 M KCl) reference electrode, and each electrodeposited-fabricated NF electrode acted as a working electrode. The alkaline electrolyte used in all tests was 1 M KOH. Before each measurement, N₂ gas was purged into the electrochemical cell to remove any amount of dissolved oxygen gas. All the experiments were repeated at least three times to confirm the obtained results. Moreover, the obtained potential values were converted to a reversible hydrogen electrode (RHE), according to the following equation:

$$E_{\text{RHE}} = E_{\text{Ag/AgCl}} + 0.059 \cdot \text{pH} + E_{\text{oAg/AgCl}} \quad (1)$$

where $E_{\text{Ag/AgCl}}$ is the potential measured with the Ag/AgCl reference electrode.

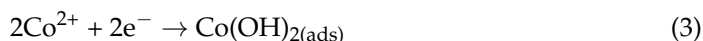
3. Results and Discussion

3.1. Electrodeposition

The electrochemical reaction rate and diffusion process are the main factors that determine the overall electrodeposition process. Mass transport limitations control the

overall process when the charge transfer reaction is fast. On the other hand, if the diffusion rate is faster than the charge transfer reaction rate, the electrochemical reaction controls the process [28].

During the electrodeposition of the precursors used in this work, the following reactions are considered [29–31]:



Moreover, recent studies have introduced a new synthetic route for metal sulfides via the formation of an $(\text{NH}_2)_2\text{CS}_s\text{-M}^{2+}\text{-OH}^-$ complex, which decomposes to the metal sulfide according to the following process [30,32]:



3.2. Structural and Morphological Evaluation

Figure 1 presents the XRD patterns of the NF, Co:S (1:0), Co:S (0:1), Co:S (1:1), Co:S (2:1), Co:S (1:2), Co:S (4:1) electrodes. The XRD analysis revealed three major peaks for the bare NF electrode at the 2θ angles of 45.2° , 52.5° , and 77° , which correspond to the (111), (200), and (220) planes of crystalline Ni, respectively. On the Co-free electrode, i.e., the Co:S (0:1) sample, there was a shift in the major peaks to 44.7° , 52.0° , and 76.5° , which are attributed to the (102), (110), and (202) crystalline planes, respectively, of the NiS phase (JCPDS file No. 02-1280) [33,34]. For the Co:S (x:y) electrodes, containing both Co and S, three major features were identified: at 44.8° , attributed to the (400) plane of the face-centered cubic Co_3O_4 structure (JCPDS No. 73-1701); 52.10° , ascribed to the (440) plane of the Co_9S_8 (PDF No.01-086-2273); and at 76.5° , attributed to the (202) crystalline plane of NiS [34–36]. No metallic phase of Ni was detected due to the formation of NiS or due to the low content (undetectable) of Ni. The XRF spectra and EDS analysis (Figures S1 and S2) also revealed the presence of sulfur, nickel, and cobalt on the as-prepared electrodes, further verifying the successful formation of Co_xS_y heterostructures according to the procedure described below (Section 2.2). These heterostructures could be responsible for the enhanced electrical conductivity and supercapacitor performance, as further discussed below on the basis of the electrochemical impedance spectroscopy (EIS) results and in agreement with relevant studies [27]. Also, it is worth noticing that S-treatment (Co:S (0:1)) did not result in any structural deformation of the NF substrate, since both samples exhibited similar lattice parameters (Table S1). However, all Co-containing samples obeyed a much higher lattice parameter, indicating the formation of new Co_xS_y phases and strain in the crystal lattice.

The mean particle size for the as-prepared electrodes was calculated using the Scherrer equation, and the obtained values are summarized in Table 1. The smallest particle size of 27.5 nm was obtained for the Co:S (1:1) electrode. The rest of the fabricated electrodes presented higher crystallite sizes, varying between 28 and 35 nm. Interestingly, the optimum electrochemical behavior (see below) was obtained for the equimolar Co:S (1:1) electrode, probably implying a structure–performance relationship; a smaller particle size could result in an extended active electrochemical zone, facilitating the oxygen evolution reaction, in accordance with relevant studies [37]. This is further discussed below, based on electrochemical and impedance spectroscopy studies.

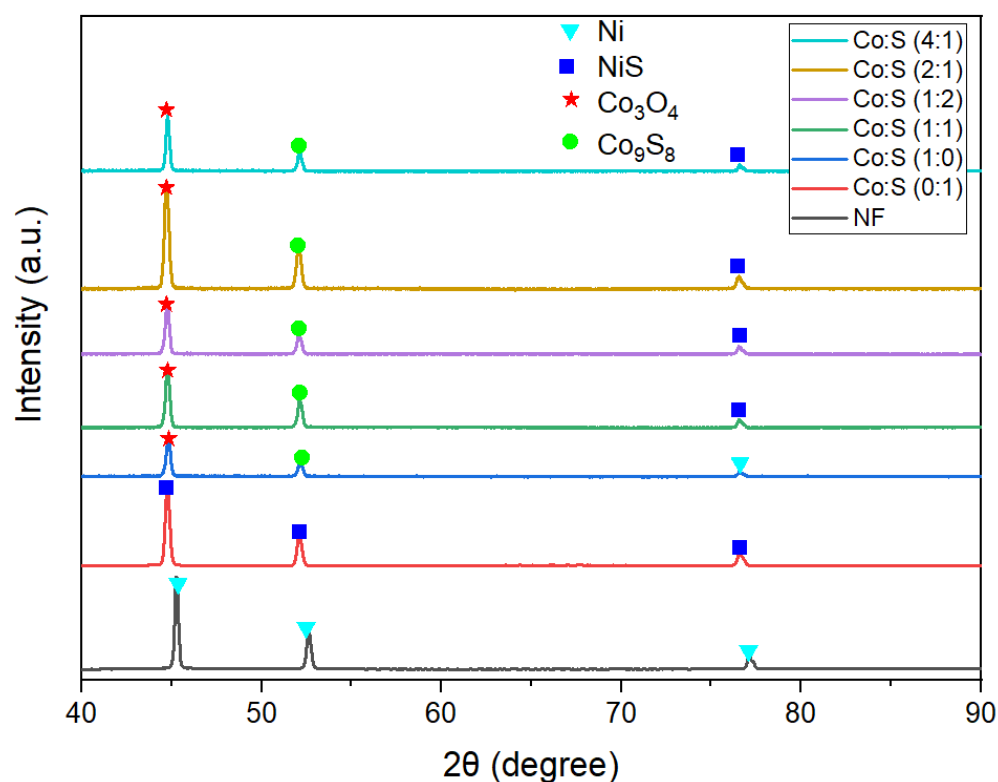


Figure 1. XRD patterns of the bare NF and Co_xS_y @NF electrodes with different Co:S molar ratios.

Table 1. Mean particle size for the NF and Co_xS_y @NF electrodes with different Co:S molar ratios.

Electrode	Mean Particle Size (nm)
NF	35.3
Co:S (1:0)	28.1
Co:S (0:1)	31.5
Co:S (1:2)	30.1
Co:S (2:1)	29.2
Co:S (4:1)	32.2
Co:S (1:1)	27.5

In Figure 2, the FE-SEM morphological analysis of the Co_xS_y @NF electrodes is presented. In the S-only electrode (Co:S (0:1)), no obvious modifications compared to the bare NF substrate were obtained (Figure 2). In the Co-rich electrodes (Co:S (2:1) and Co:S (4:1) samples), nanosheets of irregular morphology with dense agglomerations were observed (Figure 2a,b). Similarly, where the sulfur was in excess (Figure 2c), bulky structures were obtained without an apparent formation of nanosheets (Figure 2c). Efficient electro-catalysis requires an easy flow of the involved neutral and charged species toward and from the catalytic sites; thus, the above morphology, with the presence of agglomerates, corroborates well with the inferior performance of the Co-rich and S-rich electrodes for the OER (see below) [15].

Interestingly, in the case of Co_xS_y @NF electrodes with an equimolar Co:S ratio (Figure 2d–f), the formation of well-tuned 3D flower-like nanosheets was observed. This distinct morphology is most evident in higher magnification images (Figure 2e,f), where the formation of flower-like nanosheets with a vertical orientation and a thickness of ca. 7.0 nm can be observed. These findings imply the crucial effect of the Co:S ratio on the structural and morphological characteristics of the as-prepared Co_xS_y @NF electrodes, which are expected to affect the overall electrochemical performance. In other words, only the equimolar Co:S ratio results in a distinct nano-architecture of 3D flower-like nanosheets without creating agglomerates,

which can notably enhance the ESCA; the as-formed in-plane pores may bring about additional active sites, allowing a better electrolyte flow and faster OER kinetics [37].

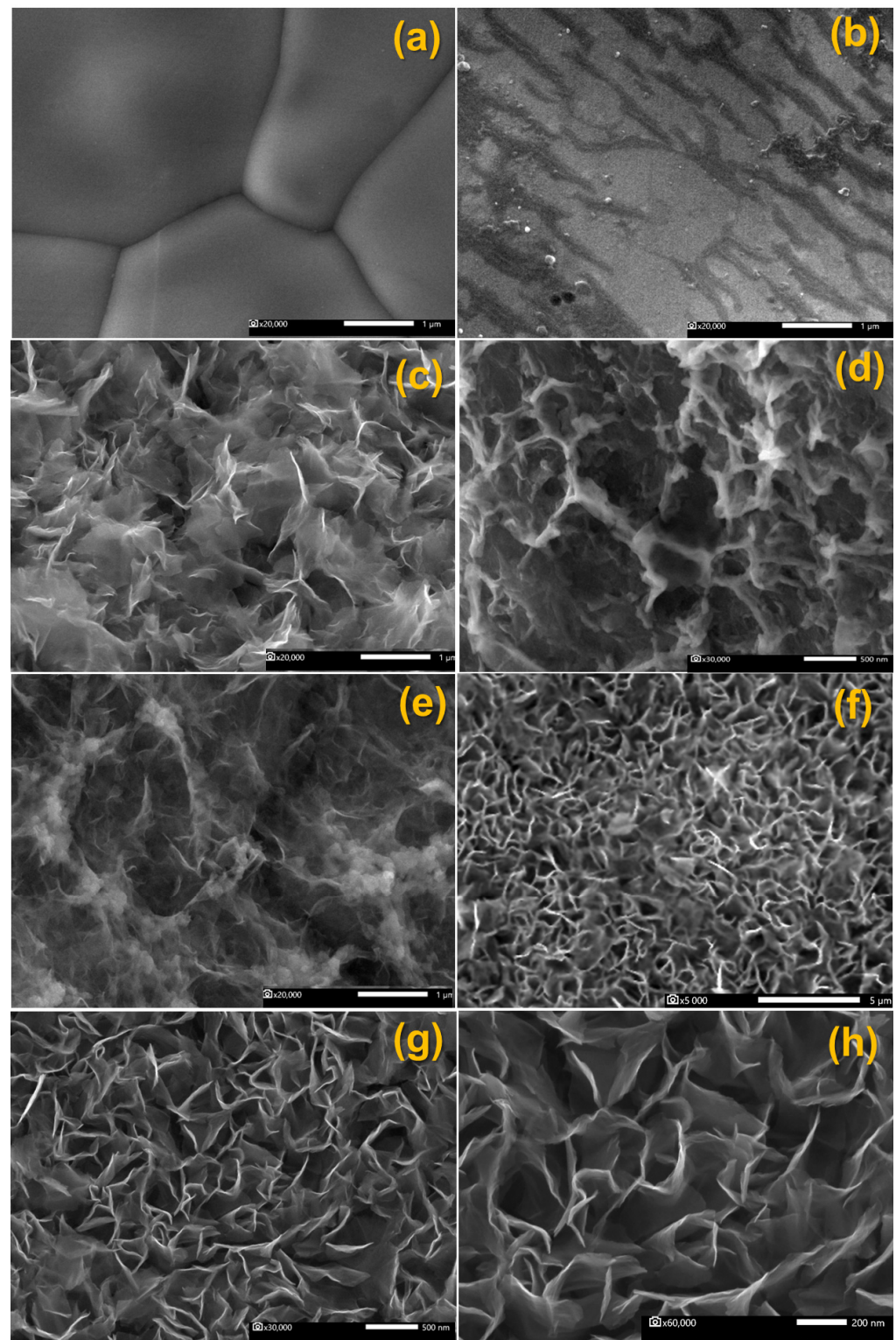
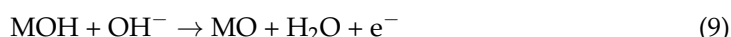


Figure 2. FE-SEM of the NF (a), Co:S (0:1) (b), Co:S (2:1) (c), Co:S (4:1) (d), Co:S (1:2) (e), Co:S (1:1) (f), Co:S (1:1) higher magnification scale (g,h).

3.3. Electrochemical Evaluation

Over the past years, several mechanisms for the OER in alkaline water electrolysis cells have been proposed [38,39]. Generally, the OER proceeds via two different routes: (a) nucleophilic water attack (WNA) or the adsorbate evolution mechanism (AEM), where MOOH (M is the active site) is initially created, and the reaction proceeds via adsorption/desorption, (b) O–O coupling, followed by O₂ evolution from the coupling of two metal-oxyl radicals with different variants [24,40,41].

The following reaction scheme is usually considered for the OER (WNA) in an alkaline medium [24]:



Finally, the overall reaction can be written as follows:



Furthermore, recent studies have proposed a new mechanism for the OER based on redox chemistry, defined as a lattice oxidation mechanism (LOM). In this mechanism, the lattice oxygen could be activated at the corresponding potential and could participate in the formation of O–O active intermediates during the OER [42–44].

In addition, when transition metal chalcogenides (TMCs), such as S, are combined with transition metals such as Co, a kinetic structural transformation of the Co_xS_y occurs during the OER [45]. An underlying dissolution of sulfur atoms promotes the oxidation of cobalt ions and facilitates the transformation of Co_xS_y nanovesicles to Co(OH)₂ and then to crystalline CoOOH, initiating the OER [46,47].

In order to explore the OER kinetics of as-prepared electrocatalysts (Figure 3a), the electrochemical polarization curves were obtained in 1 M KOH, with a scan rate of 1 mV s⁻¹ (90% iR compensation) (Figure 3a). The obtained results, summarized in Table 2, clearly show the significant impact of the Co:S ratio on the OER kinetics. When only S is deposited on NF (Co:S (0:1) sample), a significant inhibition is observed, reflected in overpotential. On the other hand, the deposition of bare cobalt over the NF substrate (Co:S (1:0) sample) has a positive effect, resulting in a lower overpotential (Figure 3a, Table 2). Notably, the fabricated electrodes containing both Co and S demonstrate lower overpotential values, implying the synergistic effect of Co_xS_y@NF composites for an enhanced OER [48]. It is evident that the Co:S (1:1) electrode, with an equimolar Co and S content, exhibits the lowest overpotential value of 0.28 V at a 10 mA cm⁻² current density, $|\eta_{10}|$, being far lower compared to 0.42 V of bare NF.

Table 2. Overpotential values ($|\eta_{10}|$) and Tafel slope in 1M KOH of all the fabricated electrodes.

Electrode	$ \eta_{10} $ (V)	Tafel Slope (mV dec ⁻¹)
NF	0.42	134 ± 0.01
Co:S (1:0)	0.31	106 ± 0.7
Co:S (0:1)	0.53	135 ± 0.7
Co:S (1:2)	0.32	113 ± 0.6
Co:S (2:1)	0.34	110 ± 0.4
Co:S (4:1)	0.3	127 ± 0.7
Co:S (1:1)	0.28	95 ± 0.3

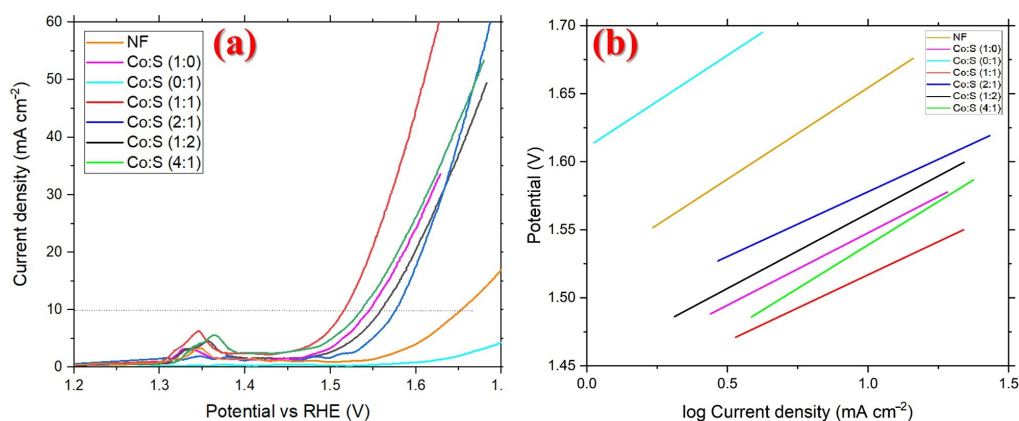


Figure 3. Electrochemical performance of the NF, Co:S (1:0), Co:S (0:1), Co:S (1:1), Co:S (2:1), Co:S (1:2), Co:S (4:1) for the OER: (a) Linear sweep voltammograms (LSV) at a scan rate of 1 mV s^{-1} in 1 M KOH ; (b) Tafel plots of the fabricated electrodes corresponding to the LSV curves.

At this point, it is also worth noting that the S-doped NF electrodes (Co:S (0:1)), where NiS is mainly detected, exhibit an even inferior performance compared to bare NF, plausibly implying the low OER reactivity of the NiS phase under the present conditions. On the other hand, the Co:S (1:0) electrode, where Co_xS_y has been detected, exhibits an adequate OER performance, most probably revealing the high reactivity of the Co_xS_y phase towards the OER reaction. Although these findings cannot exclude the possibility of the synergistic effects between the Ni_xS_x and Co_xS_y phases when both co-exist on the NF surface, they imply the pivotal effect of Co and S coexistence on the improvement in OER performance.

Afterward, the Tafel slope was determined using the linear part of the Tafel plot, according to the following equation:

$$\eta = a + b \log j \quad (13)$$

where η is the overpotential value, j is the current density, a is the fitting parameter, and b is the Tafel slope [4,16,49].

The calculated Tafel slopes of the fabricated electrodes (Figure 3b and Figure S2 and Table 2) further strengthen the findings regarding the enhanced electrocatalytic activity of the Co:S (1:1) electrode, presenting the lowest Tafel slope (95 mV dec^{-1}) for the OER. The lowest Tafel slope of the Co:S (1:1) electrode confirms its faster oxygen evolution reaction kinetics, which could be attributed to the electrode's distinct nano-architecture (Figure 2f), offering the required in-plane pores for a better electrolyte flow and an extension of the active electrocatalytic area for the OER. Moreover, the Co:S (1:1) shows excellent stability in a 30 wt% KOH solution for more than 12 h (Figure S4), demonstrating its potential for practical applications. In addition, the lower overpotential of the Co:S (1:1) at 50 mA cm^{-2} compared to the other Co_xS_y electrodes is obvious (Figure S4); this is due to the retainment of flower-like nanosheets on its surface after a prolonged stability test (Figure S5). Also, the almost unchanged XRF spectra of the Co:S (1:1) electrode, before and after the stability test, clearly reveal the stability of the aforementioned electrode (Figure S5). These findings demonstrate the stability of Co_xS_y -based electrodes in terms of their morphological and compositional characteristics, leading to an enhanced OER performance.

The superior performance of the Co:S (1:1) electrode can be further revealed through a comparison with state-of-the-art Co_xS_y -containing electrodes over NF substrates, as well as with the benchmark Ru and Ru@IrO₂ electrodes used for the OER (Table 3). It is evident that the as-prepared Co_xS_y @NF electrodes exhibit lower values compared to the Ru and Ru@IrO₂ catalysts, but are superior compared to most of the non-noble metal catalysts, offering one of the lowest Tafel slopes despite their simpler composition (monometallic Co electrodes) and facile fabrication procedure (one-step electrodeposition).

Table 3. Comparison with state-of-the-art Co- and S-containing electrodes for the OER in alkaline medium.

Electrodes	Method	Tafel Slope mV dec ⁻¹	Electrolyte	Reference
NiCo ₂ S ₄ /Ni ₃ S ₂	Hydrothermal	137	1 M KOH	[50]
NiCo-LDHs	Hydrothermal	118	1 M KOH	[51]
Co-Ni ₃ S ₂ /NF	Hydrothermal method-liquid-phase vulcanization	176	1 M KOH	[52]
CoNiS _x /NF	Sulfuration process	107	1 M KOH	[53]
NiCo ₂ S ₄ /NF	Hydrothermal	95	1 M KOH	[54]
Co ₉ S ₈ NM/NF	Hydrothermal	150	1 M KOH	[55]
NiCo ₂ S ₄ -NF	Hydrothermal	91	1 M NaOH	[56]
Ru nanoparticles	Laser-generated	70	0.5 M H ₂ SO ₄	[57]
Ru@IrO _x	Charge redistribution	69	0.05 M H ₂ SO ₄	[58]
Co:S (1:1)@NF	Electrodeposition	95	1 M KOH	This work

The enhanced OER kinetics of the Co:S (1:1) electrodes can be ascribed to the formation of flower-like nanosheets over the NF substrate (Figure 2e,f); these increase the electrochemically active area and are responsible for the high utilization ratio of electrocatalytic active sites [16]. Moreover, the absence of a binder and the direct adherence of Co and S onto the NF substrate may further account for the facile electron transportation and improved electrical conductivity, as supported by EIS experiments (see below).

Moreover, to verify our assumption that the mean particle size is closely linked to the Co/S molar ratio and, in turn, to the electrochemical performance, the Tafel slope and mean grain size are plotted in Figure 4 as a function of the Co/S ratio. Notably, the mean particle size totally coincides with the Tafel slope, implying their interrelation; the small particle size offers more electrochemical active sites, facilitating the OER kinetics. Neither Co-rich nor S-rich electrodes provide the optimum performance, maximized for the equimolar Co:S ratio of 1:1; this is in perfect agreement with the electrochemical performance results (lowest Tafel slope and overpotential values).

The double-layer capacitance (C_{DL}) and electrochemical active surface area (ESCA) were next considered in order to gain insights into the intrinsic electrocatalytic reactivity of the as-prepared electrodes. The C_{DL} , obtained via the cyclic voltammetry method, is proportional to the dependent capacitive current (J_{DL}) in the following equation:

$$J_{DL} = C_{DL} \times \frac{v}{A} \quad (14)$$

where v stands for the scan rate ($V s^{-1}$) and A for the electrode surface (cm^2) [39,59,60].

The following equation can be used to obtain the ESCA values:

$$ESCA = C_{DL} \times \frac{1}{20} \quad (15)$$

The value $20 \mu F cm^{-2}$ is the C_{DL} value of a perfectly smooth Ni electrode [61,62].

Cyclic voltammograms with scan rates of 5 to $100 mVs^{-1}$ (Figure S4) were obtained close to the open circuit potential ($\pm 50 mV$) of each electrode in a non-Faradaic region to calculate the C_{DL} values [63–65] (Figure 5, Table 4). Afterward, the C_{DL} and the ESCA values were calculated by plotting the average J_{DL} vs. scan rate and obtaining the slope.

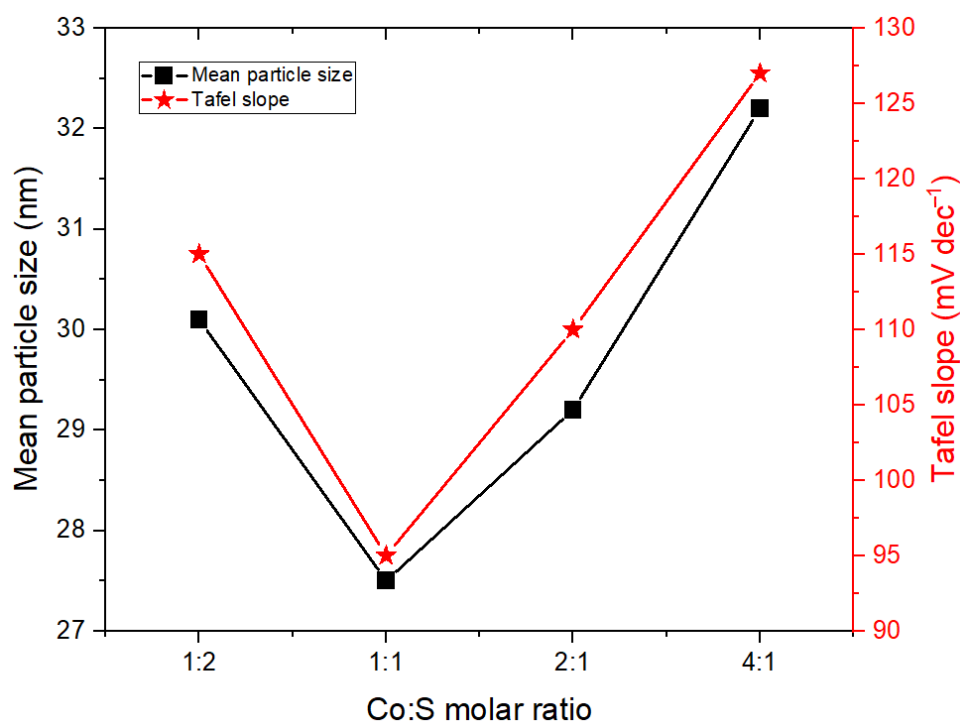


Figure 4. Co:S molar ratio vs. mean particle size and Tafel slope of the Co:S (1:1), Co:S (2:1), Co:S (1:2), Co:S (4:1) electrodes.

Table 4. Double-layer capacitance and ECSA values for the as-synthesized electrodes.

Electrode	C_{DL} Value (mF cm^{-2})	ECSA (cm^2)
NF	0.76 ± 0.13	38 ± 0.5
Co:S (1:0)	1.96 ± 0.13	98 ± 0.4
Co:S (0:1)	0.26 ± 0.01	13 ± 0.3
Co:S (1:2)	1.67 ± 0.09	83.5 ± 0.5
Co:S (2:1)	2.16 ± 0.23	108 ± 0.8
Co:S (4:1)	1.78 ± 0.19	89 ± 0.4
Co:S (1:1)	10.74 ± 0.71	537 ± 1.1

Cobalt deposition generally increases the C_{DL} and ECSA values compared to the NF reference electrode. On the other hand, sulfur deposition has a detrimental effect. Remarkably, the Co:S (1:1) electrode exhibits the best C_{DL} (10.74 mF cm^{-2}) and ECSA (537 cm^2) values, which are about one order of magnitude higher compared to the corresponding values of the NF background electrode. These findings are in line with the optimum structural (smallest particle size) and morphological (highly dispersed 3D nanosheets) characteristics of the Co:S (1:1) electrode, further corroborating the close relationship between the structural–morphological features and electrochemical performance. It is also worth noting that the high C_{DL} values of the $\text{Co}_x\text{S}_y\text{@NF}$ electrodes imply their potential use as electrodes for electrochemical supercapacitors [66,67].

Electrochemical impedance spectroscopy (EIS) measurements were next carried out to gain insights into the charge transfer and transport processes involved in the OER reaction. EIS was applied in potentiostatic mode between frequencies ranging from 10 kHz to 0.1 Hz, applying a sinusoidal alternating current (AC) potential of 10 mV (RMS). In Figure 6, the Nyquist plots of the as-prepared electrodes are presented.

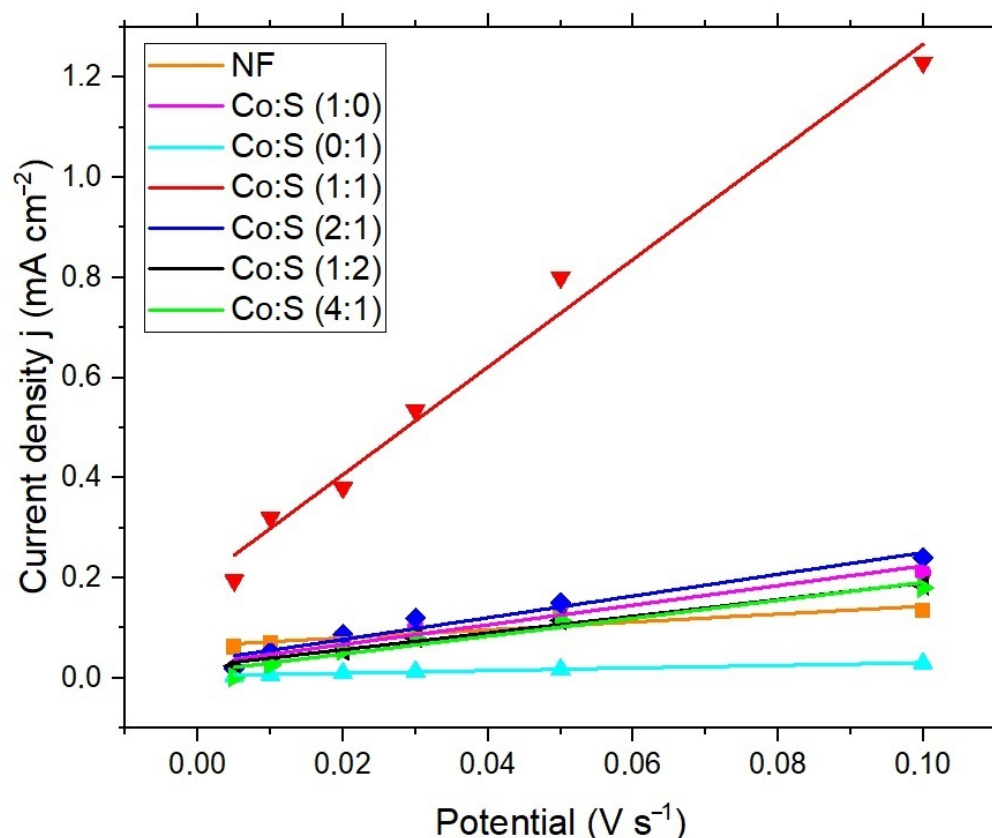


Figure 5. Average absolute current density vs. scan rate for C_{DL} estimation of the NF, Co:S (1:0), Co:S (0:1), Co:S (1:1), Co:S (2:1), Co:S (1:2), and Co:S (4:1) electrodes, at scan rates of 0.005 V s^{-1} – 0.1 V s^{-1} .

The intercept point on the Z real axis of the Nyquist plot (Figure 6), at high frequencies, depicts the electrolyte and the internal electrode's resistance (R_s) [68–70]. The gradient line achieved in low frequencies corresponds to the diffusion resistance known as the Warburg element, W [71]. The constant phase element (CPE) represents the double-layer capacitance between solid and ionic solutions [72]. Also, the charge transfer resistance (R_{ct}) reflects the difficulty the charge transfer oxygen evolution reaction has in proceeding. Table 5 summarizes the R_s and R_{ct} values of all fabricated electrodes.

Table 5. Charge transfer resistance (R_{ct}) and electronic resistance R_s of Co:S (1:0), Co:S (0:1), Co:S (1:2), Co:S (2:1), Co:S (4:1), and Co:S (1:1) electrodes.

Electrode	R_s (Ω)	R_{ct} (Ω)
Co:S (1:0)	2.1 ± 0.003	39.4 ± 9.5
Co:S (0:1)	2.8 ± 0.004	$155,566 \pm 3449$
Co:S (1:2)	2.5 ± 0.004	1.9 ± 0.2
Co:S (2:1)	2 ± 0.009	521 ± 7
Co:S (4:1)	2.3 ± 0.01	0.75 ± 0.03
Co:S (1:1)	2.2 ± 0.008	0.000006 ± 0.008

It is apparent that the Co:S (1:1) electrode provides, by far, the lower R_{ct} , resulting in an enhancement in the OER kinetics. Moreover, at higher frequencies, the Co:S (1:1) electrode exhibits the Warburg line (Figure 6), implying a better capacity and improved conductivity [71,73]. It should be noted, however, that no significant differences can be observed between the R_s values of Co-containing samples, implying the crucial role of the active metal phase (Co) in determining the electrode's resistance. Hence, based on the present results, the excellent electrochemical performance of the Co:S (1:1) electrode could

be mainly ascribed to its low R_{ct} , thereby accelerating the charge transfer oxygen evolution reaction.

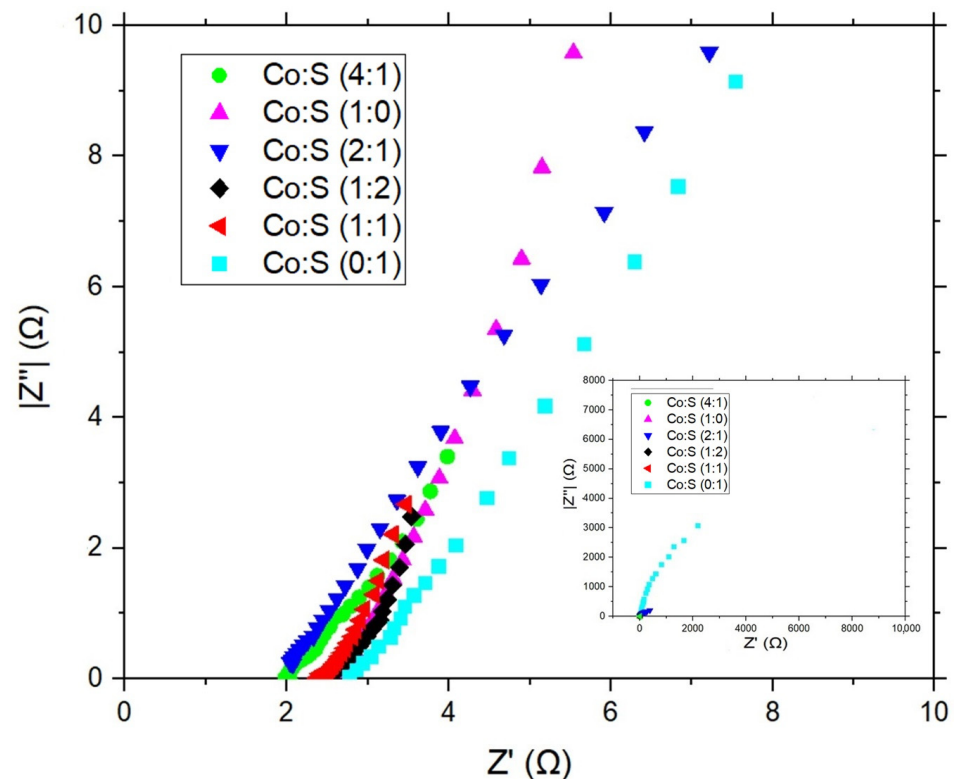


Figure 6. Zoomed in Nyquist plot of Co:S (1:0), Co:S (0:1), Co:S (1:2), Co:S (2:1), Co:S (4:1), and Co:S (1:1) electrodes in 1M KOH. Inset: zoomed out Nyquist plot.

4. Conclusions

The present work systematically explored the impact of the Co/S molar ratio on the OER kinetics and electrochemical performance of $\text{Co}_x\text{S}_y@\text{NF}$ electrodes. Thiourea and cobalt nitrate precursors at different stoichiometric concentrations were used to fabricate $\text{Co}_x\text{S}_y@\text{NF}$ heterostructures through the electrodeposition method.

Notably, it was found that the Co:S ratio profoundly influenced the structure and morphology of the as-prepared electrodes and, in turn, their OER kinetics. The $\text{Co}_x\text{S}_y@\text{NF}$ electrode with a Co:S ratio of 1:1 exhibited the lowest overpotential value at 10 mA cm^{-2} (0.28 V) and a Tafel slope of 95 mV dec^{-1} , offering, in addition, a high double-layer capacitance (C_{DL}) of 10.74 mF cm^{-2} . Electrochemical impedance spectroscopy confirmed the key role of the Co:S ratio on charge transfer resistance, which is substantially decreased at a Co:S molar ratio of 1:1. Structural and morphological analysis disclosed that the $\text{Co}_x\text{S}_y@\text{NF}$ electrocatalyst with an equimolar Co:S ratio presented a 3D flower-like nanosheet morphology, offering the smallest particle size and the highest electrochemical active area, which are both conducive to improving the OER kinetics.

The enhanced electrocatalytic activity, stability, facile synthesis route, and free-of-binders fabrication procedure render $\text{Co}_x\text{S}_y@\text{NF}$ electrodes a promising earth-abundant, noble metal-free, bifunctional type of electrocatalyst for the OER in alkaline water electrolysis cells.

Supplementary Materials: The following supporting information can be downloaded at: <https://www.mdpi.com/article/10.3390/surfaces6040033/s1>, Figure S1. XRF analysis of the Co:S (1:1) electrode; Figure S2. EDS analysis of the as-prepared Co:S electrodes; Figure S3. Tafel slope of the fabricated electrodes in 1 M KOH electrolyte; Figure S4. Stability test of all the fabricated electrodes; Figure S5. FE-SEM of the Co:S (2:1) (a), Co:S (4:1) (b), Co:S (1:2) (c), Co:S (1:1) after

prolonged stability tests. XRF spectra of the Co:S (1:1) electrode before and after the OER stability test; Figure S6. Capacitance double layer measurements with cyclic voltammetry; Figure S7. EIS fitting data and equivalent circuits for the as-prepared electrodes; Table S1. Lattice parameters of the as-prepared electrodes.

Author Contributions: Conceptualization, I.P. and M.K.; methodology, I.P. and M.K.; validation, I.P., M.K. and N.P.; formal analysis, I.P., M.K.; investigation, I.P.; resources, M.K., P.A.L. and G.E.M.; data curation, I.P.; writing—original draft preparation, I.P.; writing—review and editing, I.P., M.K., G.E.M.; visualization, I.P. and M.K.; supervision, M.K., G.E.M. and P.A.L.; project administration, M.K.; funding acquisition, M.K., G.E.M. and P.A.L. All authors have read and agreed to the published version of the manuscript.

Funding: This research has received funding from the European Union under grant agreement No 101099717–ECOLEFINS project. Views and opinions expressed are, however, those of the author(s) only and do not necessarily reflect those of the European Union or European Innovation Council and SMEs Executive Agency (EISMEA) granting authority. Neither the European Union nor the granting authority can be held responsible for them. PL, NP acknowledge financial support from the European Union’s Horizon 2020 research and innovation program under grant agreement no 871124 Laserlab-Europe. The authors would like to acknowledge the HELLAS-CH national infrastructure (MIS 5002735) implemented under “Action for Strengthening Research and Innovation Infrastructures,” funded by the Operational Programme “Competitiveness, Entrepreneurship, and Innovation” (NSRF 2014-2020) and co-financed by Greece and the European Union (European Regional Development Fund).

Institutional Review Board Statement: Not applicable.

Informed Consent Statement: Not applicable.

Data Availability Statement: The data supporting the findings of this study are available in the form of Tables/Figures within the article and its Supplementary Materials. The raw data are available from the corresponding authors upon reasonable request.

Acknowledgments: The authors want to acknowledge A. Manousaki for the field emission SEM.

Conflicts of Interest: The authors declare no conflict of interest.

References

1. Bockris, J.O.; Veziroglu, T.N. Estimates of the price of hydrogen as a medium for wind and solar sources. *Int. J. Hydrogen Energy* **2007**, *32*, 1605–1610. [[CrossRef](#)]
2. Guo, Y.; Shang, C.; Li, J.; Wang, E. Recent development of hydrogen evolution, oxygen evolution and oxygen reduction reaction. *Sci. Sin. Chim.* **2018**, *48*, 926–940. [[CrossRef](#)]
3. Wei, Y.; Wang, M.; Fu, W.; Wei, L.; Zhao, X.; Zhou, X.; Ni, M.; Wang, H. Highly active and durable catalyst for hydrogen generation by the NaBH₄ hydrolysis reaction: CoWB/NF nanodendrite with an acicular array structure. *J. Alloys Compd.* **2020**, *836*, 155429. [[CrossRef](#)]
4. Poimenidis, I.A.; Papakosta, N.; Klini, A.; Farsari, M.; Konsolakis, M.; Loukakos, P.A.; Moustazis, S. Electrodeposited Ni foam electrodes for increased hydrogen production in alkaline electrolysis. *Fuel* **2023**, *342*, 127798. [[CrossRef](#)]
5. Guan, D.; Wang, B.; Zhang, J.; Shi, R.; Jiao, K.; Li, L.; Wang, Y.; Xie, B.; Zhang, Q.; Yu, J.; et al. Hydrogen society: From present to future. *Energy Environ. Sci.* **2023**, *16*, 4926–4943. [[CrossRef](#)]
6. McCrory, C.C.L.; Jung, S.; Ferrer, I.M.; Chatman, S.M.; Peters, J.C.; Jaramillo, T.F. Benchmarking Hydrogen Evolving Reaction and Oxygen Evolving Reaction Electrocatalysts for Solar Water Splitting Devices. *J. Am. Chem. Soc.* **2015**, *137*, 4347–4357. [[CrossRef](#)]
7. Han, G.-Q.; Shang, X.; Lu, S.-S.; Dong, B.; Li, X.; Liu, Y.-R.; Hu, W.; Zeng, J.-B.; Chai, Y.-M.; Liu, C.-G. Electrodeposited MoS_x films assisted by liquid crystal template with ultrahigh electrocatalytic activity for hydrogen evolution reaction. *Int. J. Hydrogen Energy* **2017**, *42*, 5132–5138. [[CrossRef](#)]
8. Wu, G.; Santandreu, A.; Kellogg, W.; Gupta, S.; Ogoke, O.; Zhang, H.; Wang, H.-L.; Dai, L. Carbon nanocomposite catalysts for oxygen reduction and evolution reactions: From nitrogen doping to transition-metal addition. *Nano Energy* **2016**, *29*, 83–110. [[CrossRef](#)]
9. Kanan, M.W.; Nocera, D.G. In Situ Formation of an Oxygen-Evolving Catalyst in Neutral Water Containing Phosphate and Co²⁺. *Science (1979)* **2008**, *321*, 1072–1075. [[CrossRef](#)]
10. Song, J.; Wei, C.; Huang, Z.-F.; Liu, C.; Zeng, L.; Wang, X.; Xu, Z. A review on fundamentals for designing oxygen evolution electrocatalysts. *Chem. Soc. Rev.* **2020**, *49*, 2196–2214. [[CrossRef](#)]

11. Imran Anwar, M.; Manzoor, S.; Ma, L.; Asad, M.; Zhang, W.; Shafiq, Z.; Ashiq, M.-N.; Yang, G. Nitrogen-rich three-dimensional metal-organic framework microrods as an efficient electrocatalyst for oxygen evolution reaction and supercapacitor applications. *Fuel* **2023**, *331*, 125746. [[CrossRef](#)]
12. Jung, S.; McCrory, C.C.L.; Ferrer, I.M.; Peters, J.C.; Jaramillo, T.F. Benchmarking nanoparticulate metal oxide electrocatalysts for the alkaline water oxidation reaction. *J. Mater. Chem. A Mater.* **2016**, *4*, 3068–3076. [[CrossRef](#)]
13. Chi, J.-Q.; Shang, X.; Liang, F.; Dong, B.; Li, X.; Liu, Y.-R.; Yan, K.-L.; Gao, W.-K.; Chai, Y.-M.; Liu, C.-G. Facile synthesis of pyrite-type binary nickel iron diselenides as efficient electrocatalyst for oxygen evolution reaction. *Appl. Surf. Sci.* **2017**, *401*, 17–24. [[CrossRef](#)]
14. Sarfraz, B.; Bashir, I.; Rauf, A. CuS/NiFe-LDH/NF as a Bifunctional Electrocatalyst for Hydrogen Evolution (HER) and Oxygen Evolution Reactions (OER). *Fuel* **2023**, *337*, 127253. [[CrossRef](#)]
15. Shit, S.; Chhetri, S.; Jang, W.; Murmu, N.C.; Koo, H.; Samanta, P.; Kuila, T. Cobalt Sulfide/Nickel Sulfide Heterostructure Directly Grown on Nickel Foam: An Efficient and Durable Electrocatalyst for Overall Water Splitting Application. *ACS Appl. Mater. Interfaces* **2018**, *10*, 27712–27722. [[CrossRef](#)] [[PubMed](#)]
16. Kale, S.B.; Lokhande, A.C.; Pujari, R.B.; Lokhande, C.D. Cobalt sulfide thin films for electrocatalytic oxygen evolution reaction and supercapacitor applications. *J. Colloid Interface Sci.* **2018**, *532*, 491–499. [[CrossRef](#)]
17. Kuai, L.; Geng, J.; Chen, C.; Kan, E.; Liu, Y.; Wang, Q.; Geng, B. A Reliable Aerosol-Spray-Assisted Approach to Produce and Optimize Amorphous Metal Oxide Catalysts for Electrochemical Water Splitting. *Angew. Chem. Int. Ed.* **2014**, *53*, 7547–7551. [[CrossRef](#)]
18. Smith, R.D.L.; Prévot, M.S.; Fagan, R.D.; Zhang, Z.; Sedach, P.A.; Siu, M.K.J.; Trudel, S.; Berlinguette, C. Photochemical Route for Accessing Amorphous Metal Oxide Materials for Water Oxidation Catalysis. *Science* **2013**, *340*, 60–63. [[CrossRef](#)]
19. Borthakur, P.; Boruah, P.K.; Das, M.R.; Ibrahim, M.M.; Altalhi, T.; El-Sheshtawy, H.S.; Szunerits, S.; Boukherroub, R.; Amin, M. CoS₂ Nanoparticles Supported on rGO, g-C₃N₄, BCN, MoS₂, and WS₂ Two-Dimensional Nanosheets with Excellent Electrocatalytic Performance for Overall Water Splitting: Electrochemical Studies and DFT Calculations. *ACS Appl. Energy Mater.* **2021**, *4*, 1269–1285. [[CrossRef](#)]
20. Poimenidis, I.A.; Lykaki, M.; Moustazis, S.; Loukakos, P.; Konsolakis, M. One-step solvothermal growth of NiO nanoparticles on nickel foam as a highly efficient electrocatalyst for hydrogen evolution reaction. *Mater. Chem. Phys.* **2023**, *305*, 128007. [[CrossRef](#)]
21. Surendran, S.; Shanmugapriya, S.; Lee, Y.S.; Sim, U.; Selvan, R.K. Carbon-Enriched Cobalt Phosphide with Assorted Nanostructure as a Multifunctional Electrode for Energy Conversion and Storage Devices. *ChemistrySelect* **2018**, *3*, 12303–12313. [[CrossRef](#)]
22. Prabakaran, K.; Lokanathan, M.; Kakade, B. Three dimensional flower like cobalt sulfide (CoS)/functionalized MWCNT composite catalyst for efficient oxygen evolution reactions. *Appl. Surf. Sci.* **2019**, *466*, 830–836. [[CrossRef](#)]
23. Poimenidis, I.A.; Papakosta, N.; Klini, A.; Farsari, M.; Moustazis, S.D.; Konsolakis, M.; Loukakos, P. Ni foam electrodes decorated with Ni nanoparticles via pulsed laser deposition for efficient hydrogen evolution reaction. *Mater. Sci. Eng. B* **2024**, *299*, 116922. [[CrossRef](#)]
24. Zhao, Y.; Adiyeri Saseendran, D.P.; Huang, C.; Triana, C.A.; Marks, W.R.; Chen, H.; Zhao, H.; Patzke, G.-R. Oxygen Evolution/Reduction Reaction Catalysts: From In Situ Monitoring and Reaction Mechanisms to Rational Design. *Chem. Rev.* **2023**, *123*, 6257–6358. [[CrossRef](#)]
25. Wang, M.; Zhang, L.; He, Y.; Zhu, H. Recent advances in transition-metal-sulfide-based bifunctional electrocatalysts for overall water splitting. *J. Mater. Chem. A Mater.* **2021**, *9*, 5320–5363. [[CrossRef](#)]
26. Zhu, Y.; Song, L.; Song, N.; Li, M.; Wang, C.; Lu, X. Bifunctional and Efficient CoS₂-@MoS₂ Core-Shell Nanofiber Electrocatalyst for Water Splitting. *ACS Sustain. Chem. Eng.* **2019**, *7*, 2899–2905. [[CrossRef](#)]
27. Elshahawy, A.M.; Li, X.; Zhang, H.; Hu, Y.; Ho, K.H.; Guan, C.; Wang, J. Controllable MnCo₂S₄ nanostructures for high performance hybrid supercapacitors. *J. Mater. Chem. A Mater.* **2017**, *5*, 7494–7506. [[CrossRef](#)]
28. Yu, Y. Study on Electrochemistry and Nucleation Process of Nickel Electrodeposition. *Int. J. Electrochem. Sci.* **2017**, *12*, 485–495. [[CrossRef](#)]
29. Shi, J.; Li, X.; He, G.; Zhang, L.; Li, M. Electrodeposition of high-capacitance 3D CoS/graphene nanosheets on nickel foam for high-performance aqueous asymmetric supercapacitors. *J. Mater. Chem. A Mater.* **2015**, *3*, 20619–20626. [[CrossRef](#)]
30. Sultana, U.K.; He, T.; Du, A.; O'Mullane, A.P. An amorphous dual action electrocatalyst based on oxygen doped cobalt sulfide for the hydrogen and oxygen evolution reactions. *RSC Adv.* **2017**, *7*, 54995–55004. [[CrossRef](#)]
31. Jiang, S.P.; Chen, Y.Z.; You, J.K.; Chen, T.X.; Tseung, A.C.C. Reactive Deposition of Cobalt Electrodes: I. Experimental. *J. Electrochem. Soc.* **1990**, *137*, 3374–3380. [[CrossRef](#)]
32. Garcia-Valenzuela, J.A. Simple Thiourea Hydrolysis or Intermediate Complex Mechanism? Taking up the Formation of Metal Sulfides from Metal-Thiourea Alkaline Solutions. *Comments Inorg. Chem.* **2017**, *37*, 99–115. [[CrossRef](#)]
33. Zhang, J.; Xu, C.; Zhang, D.; Zhao, J.; Zheng, S.; Su, H.; Wei, F.; Yuan, B.; Fernandez, C. Facile Synthesis of a Nickel Sulfide (NiS) Hierarchical Flower for the Electrochemical Oxidation of H₂O₂ and the Methanol Oxidation Reaction (MOR). *J. Electrochem. Soc.* **2017**, *164*, B92–B96. [[CrossRef](#)]
34. Liu, S.; Shi, Q.; Tong, J.; Li, S.; Li, M. Controlled synthesis of spherical α -NiS and urchin-like β -NiS microstructures. *J. Exp. Nanosci.* **2014**, *9*, 475–481. [[CrossRef](#)]

35. Yan, K.-L.; Shang, X.; Li, Z.; Dong, B.; Chi, J.-Q.; Liu, Y.-R.; Gao, W.-K.; Chai, Y.-M.; Liu, C.-G. Facile synthesis of binary NiCoS nanorods supported on nickel foam as efficient electrocatalysts for oxygen evolution reaction. *Int. J. Hydrogen Energy* **2017**, *42*, 17129–17135. [[CrossRef](#)]
36. Samal, R.; Mondal, S.; Gangan, A.S.; Chakraborty, B.; Rout, C.S. Comparative electrochemical energy storage performance of cobalt sulfide and cobalt oxide nanosheets: Experimental and theoretical insights from density functional theory simulations. *Phys. Chem. Chem. Phys.* **2020**, *22*, 7903–7911. [[CrossRef](#)] [[PubMed](#)]
37. Huang, S.; He, Q.; Liu, M.; An, H.; Hou, L. Controlled synthesis of porous nanosheets-assembled peony-like cobalt nickel selenides for triiodide reduction in dye-sensitized solar cells. *J. Alloys Compd.* **2020**, *818*, 152817. [[CrossRef](#)]
38. Shervedani, R.K.; Madram, A.R. Kinetics of hydrogen evolution reaction on nanocrystalline electrodeposited Ni₆₂Fe₃₅C₃ cathode in alkaline solution by electrochemical impedance spectroscopy. *Electrochim. Acta* **2007**, *53*, 426–433. [[CrossRef](#)]
39. Hosseini, M.G.; Momeni, M.M.; Faraji, M. Highly Active Nickel Nanoparticles Supported on TiO₂ Nanotube Electrodes for Methanol Electrooxidation. *Electroanalysis* **2010**, *22*, 2620–2625. [[CrossRef](#)]
40. Shaffer, D.W.; Xie, Y.; Concepcion, J.J. O–O bond formation in ruthenium-catalyzed water oxidation: Single-site nucleophilic attack vs. O–O radical coupling. *Chem. Soc. Rev.* **2017**, *46*, 6170–6193. [[CrossRef](#)]
41. Craig, M.J.; Coulter, G.; Dolan, E.; Soriano-López, J.; Mates-Torres, E.; Schmitt, W.; Melchor, M.-G. Universal scaling relations for the rational design of molecular water oxidation catalysts with near-zero overpotential. *Nat. Commun.* **2019**, *10*, 4993. [[CrossRef](#)] [[PubMed](#)]
42. Zhao, M.; Zheng, X.; Cao, C.; Lu, Q.; Zhang, J.; Wang, H.; Huang, Z.; Cao, Y.; Wang, Y.; Deng, Y. Lattice oxygen activation in disordered rocksalts for boosting oxygen evolution. *Phys. Chem. Chem. Phys.* **2023**, *25*, 4113–4120. [[CrossRef](#)]
43. Zhu, Y.; Tahini, H.A.; Hu, Z.; Chen, Z.; Zhou, W.; Komarek, A.C.; Lin, Q.; Lin, H.-J.; Chen, C.-T.; Zhong, Y.; et al. Boosting Oxygen Evolution Reaction by Creating Both Metal Ion and Lattice-Oxygen Active Sites in a Complex Oxide. *Adv. Mater.* **2020**, *32*, 1905025. [[CrossRef](#)]
44. Yoo, J.S.; Rong, X.; Liu, Y.; Kolpak, A.M. Role of Lattice Oxygen Participation in Understanding Trends in the Oxygen Evolution Reaction on Perovskites. *ACS Catal.* **2018**, *8*, 4628–4636. [[CrossRef](#)]
45. Cao, D.; Liu, D.; Chen, S.; Moses, O.A.; Chen, X.; Xu, W.; Wu, C.; Zheng, L.; Chu, S.; Jiang, H.; et al. Operando X-ray spectroscopy visualizing the chameleon-like structural reconstruction on an oxygen evolution electrocatalyst. *Energy Environ. Sci.* **2021**, *14*, 906–915. [[CrossRef](#)]
46. Fan, K.; Zou, H.; Lu, Y.; Chen, H.; Li, F.; Liu, J.; Sun, L.; Tong, L.; Toney, M.; Sui, M.; et al. Direct Observation of Structural Evolution of Metal Chalcogenide in Electrocatalytic Water Oxidation. *ACS Nano* **2018**, *12*, 12369–12379. [[CrossRef](#)] [[PubMed](#)]
47. Wang, M.; Dong, C.-L.; Huang, Y.-C.; Shen, S. Operando Spectral and Electrochemical Investigation into the Heterophase Stimulated Active Species Transformation in Transition-Metal Sulfides for Efficient Electrocatalytic Oxygen Evolution. *ACS Catal.* **2020**, *10*, 1855–1864. [[CrossRef](#)]
48. Li, M.; Xu, Z.; Li, Y.; Wang, J.; Zhong, Q. In situ fabrication of cobalt/nickel sulfides nanohybrid based on various sulfur sources as highly efficient bifunctional electrocatalysts for overall water splitting. *Nano Sel.* **2022**, *3*, 147–156. [[CrossRef](#)]
49. Poimenidis, I.A.; Papakosta, N.; Manousaki, A.; Klini, A.; Farsari, M.; Moustazis, S.D.; Loukakos, P. Electrodeposited laser-nanostructured electrodes for increased hydrogen production. *Int. J. Hydrogen Energy* **2022**, *47*, 9527–9536. [[CrossRef](#)]
50. Wang, Y.; Chen, N.; Du, X.; Han, X.; Zhang, X. Transition metal atoms M (M = Mn, Fe, Cu, Zn) doped nickel-cobalt sulfides on the Ni foam for efficient oxygen evolution reaction and urea oxidation reaction. *J. Alloys Compd.* **2022**, *893*, 162269. [[CrossRef](#)]
51. Liu, B.; Zhang, M.; Wang, Y.; Chen, Z.; Yan, K. Facile synthesis of defect-rich ultrathin NiCo-LDHs, NiMn-LDHs and NiCoMn-LDHs nanosheets on Ni foam for enhanced oxygen evolution reaction performance. *J. Alloys Compd.* **2021**, *852*, 156949. [[CrossRef](#)]
52. Qin, J.-F.; Yang, M.; Hou, S.; Dong, B.; Chen, T.-S.; Ma, X.; Xie, J.-X.; Zhou, Y.-N.; Nan, J.; Chai, Y.-M. Copper and cobalt co-doped Ni₃S₂ grown on nickel foam for highly efficient oxygen evolution reaction. *Appl. Surf. Sci.* **2020**, *502*, 144172. [[CrossRef](#)]
53. Zhang, R.-L.; Duan, J.-J.; Feng, J.-J.; Mei, L.-P.; Zhang, Q.-L.; Wang, A.-J. Walnut kernel-like iron-cobalt-nickel sulfide nanosheets directly grown on nickel foam: A binder-free electrocatalyst for high-efficiency oxygen evolution reaction. *J. Colloid Interface Sci.* **2021**, *587*, 141–149. [[CrossRef](#)] [[PubMed](#)]
54. Min, K.; Yoo, R.; Kim, S.; Kim, H.; Shim, S.E.; Lim, D.; Baeck, S.-H. Facile synthesis of P-doped NiCo₂S₄ nanoneedles supported on Ni foam as highly efficient electrocatalysts for alkaline oxygen evolution reaction. *Electrochim. Acta* **2021**, *396*, 139236. [[CrossRef](#)]
55. Gao, W.-K.; Qin, J.-F.; Wang, K.; Yan, K.-L.; Liu, Z.-Z.; Lin, J.-H.; Chai, Y.-M.; Liu, C.-G.; Dong, B. Facile synthesis of Fe-doped Co₉S₈ nano-microspheres grown on nickel foam for efficient oxygen evolution reaction. *Appl. Surf. Sci.* **2018**, *454*, 46–53. [[CrossRef](#)]
56. Yin, X.; Sun, G.; Wang, L.; Bai, L.; Su, L.; Wang, Y.; Du, Q.; Shao, G. 3D hierarchical network NiCo₂S₄ nanoflakes grown on Ni foam as efficient bifunctional electrocatalysts for both hydrogen and oxygen evolution reaction in alkaline solution. *Int. J. Hydrogen Energy* **2017**, *42*, 25267–25276. [[CrossRef](#)]
57. Wang, J.-Q.; Xi, C.; Wang, M.; Shang, L.; Mao, J.; Dong, C.-K.; Liu, H.; Kulinich, S.-A.; Du, X.-W. Laser-Generated Grain Boundaries in Ruthenium Nanoparticles for Boosting Oxygen Evolution Reaction. *ACS Catal.* **2020**, *10*, 12575–12581. [[CrossRef](#)]
58. Shan, J.; Guo, C.; Zhu, Y.; Chen, S.; Song, L.; Jaroniec, M.; Zheng, Y.; Qiao, S.-Z. Charge-Redistribution-Enhanced Nanocrystalline Ru@IrOx Electrocatalysts for Oxygen Evolution in Acidic Media. *Chem* **2019**, *5*, 445–459. [[CrossRef](#)]
59. Burke, L.D.; Twomey, T.A.M. Voltammetric behaviour of nickel in base with particular reference to thick oxide growth. *J. Electroanal. Chem. Interfacial Electrochem.* **1984**, *162*, 101–119. [[CrossRef](#)]

60. Chandrasekaran, P.; Edison, T.N.J.I.; Sethuraman, M.G. Electrocatalytic study of carbon dots/Nickel iron layered double hydroxide composite for oxygen evolution reaction in alkaline medium. *Fuel* **2022**, *320*, 123947. [[CrossRef](#)]
61. Navarro-Flores, E.; Chong, Z.; Omanovic, S. Characterization of Ni, NiMo, NiW and NiFe electroactive coatings as electrocatalysts for hydrogen evolution in an acidic medium. *J. Mol. Catal. A Chem.* **2005**, *226*, 179–197. [[CrossRef](#)]
62. Li, X.; Liu, P.F.; Zhang, L.; Zu, M.Y.; Yang, Y.X.; Yang, H.G. Enhancing alkaline hydrogen evolution reaction activity through Ni-Mn₃O₄ nanocomposites. *Chem. Commun.* **2016**, *52*, 10566–10569. [[CrossRef](#)]
63. McCrory, C.C.L.; Jung, S.; Peters, J.C.; Jaramillo, T.F. Benchmarking heterogeneous electrocatalysts for the oxygen evolution reaction. *J. Am. Chem. Soc.* **2013**, *135*, 16977–16987. [[CrossRef](#)]
64. Poimenidis, I.A.; Tsanakas, M.D.; Papakosta, N.; Klini, A.; Farsari, M.; Moustazis, S.D.; Loukakos, P.A. Enhanced hydrogen production through alkaline electrolysis using laser-nanostructured nickel electrodes. *Int. J. Hydrogen Energy* **2021**, *46*, 37162–37173. [[CrossRef](#)]
65. Symes, D.; Taylor-Cox, C.; Holyfield, L.; Al-Duri, B.; Dhir, A. Feasibility of an oxygen-getter with nickel electrodes in alkaline electrolyzers. *Mater. Renew. Sustain. Energy* **2014**, *3*, 27. [[CrossRef](#)]
66. Edison, T.N.J.I.; Atchudan, R.; Karthik, N.; Ganesh, K.; Xiong, D.; Lee, Y.R. A novel binder-free electro-synthesis of hierarchical nickel sulfide nanostructures on nickel foam as a battery-type electrode for hybrid-capacitors. *Fuel* **2020**, *276*, 118077. [[CrossRef](#)]
67. Huang, H.; Deng, X.; Yan, L.; Wei, G.; Zhou, W.; Liang, X.; Guo, J. One-Step Synthesis of Self-Supported Ni₃S₂/NiS Composite Film on Ni Foam by Electrodeposition for High-Performance Supercapacitors. *Nanomaterials* **2019**, *9*, 1718. [[CrossRef](#)]
68. Chen, J.; Wang, Z.; Mu, J.; Ai, B.; Zhang, T.; Ge, W.; Zhang, L. Enhanced lithium storage capability enabled by metal nickel dotted NiO-graphene composites. *J. Mater. Sci.* **2019**, *54*, 1475–1487. [[CrossRef](#)]
69. Siddiqui, S.-E.-T.; Rahman, M.d.A.; Kim, J.-H.; Sharif, S.B.; Paul, S. A Review on Recent Advancements of Ni-NiO Nanocomposite as an Anode for High-Performance Lithium-Ion Battery. *Nanomaterials* **2022**, *12*, 2930. [[CrossRef](#)]
70. Chia, X.; Ambrosi, A.; Sofer, Z.; Luxa, J.; Pumera, M. Catalytic and Charge Transfer Properties of Transition Metal Dichalcogenides Arising from Electrochemical Pretreatment. *ACS Nano* **2015**, *9*, 5164–5179. [[CrossRef](#)]
71. Agudosi, E.S.; Abdullah, E.C.; Numan, A.; Mubarak, N.M.; Aid, S.R.; Benages-Vilau, R.; Romero, P.-G.; Khalid, M.; Omar, N. Fabrication of 3D binder-free graphene NiO electrode for highly stable supercapattery. *Sci. Rep.* **2020**, *10*, 11214. [[CrossRef](#)] [[PubMed](#)]
72. Conway, B.E.; Birss, V.; Wojtowicz, J. The role and utilization of pseudocapacitance for energy storage by supercapacitors. *J. Power Source* **1997**, *66*, 1–14. [[CrossRef](#)]
73. Ge, J.; Wu, J.; Fan, L.; Bao, Q.; Dong, J.; Jia, J.; Guo, Y.; Lin, J. Hydrothermal synthesis of CoMoO₄/Co_{1-x}S hybrid on Ni foam for high-performance supercapacitors. *J. Energy Chem.* **2018**, *27*, 478–485. [[CrossRef](#)]

Disclaimer/Publisher’s Note: The statements, opinions and data contained in all publications are solely those of the individual author(s) and contributor(s) and not of MDPI and/or the editor(s). MDPI and/or the editor(s) disclaim responsibility for any injury to people or property resulting from any ideas, methods, instructions or products referred to in the content.